Milliner Christopher (Orcid ID: 0000-0002-3790-595X)

Burgmann Roland (Orcid ID: 0000-0002-3560-044X)

Inbal Asaf (Orcid ID: 0000-0001-8848-7279)

Wang Teng (Orcid ID: 0000-0003-3729-0139)

Title: Resolving the Kinematics and Moment Release of Early Afterslip within the First Hours following the 2016 M_w 7.1 Kumamoto Earthquake: Implications for the Shallow Slip Deficit and Frictional Behavior of Aseismic Creep

Author list: C., Milliner[1*], R., Bürgmann[2], A., Inbal[3], T., Wang[4], C., Liang[5]

Affiliations

[1] Jet Propulsion Laboratory, California Institute of Technology, Pasadena, CA 91109, USA.

[2] Department of Earth and Planetary Science, University of California Berkeley, Berkeley, CA 94720, USA.

[3] Porter School of the Environment and Earth Sciences, Tel Aviv University, Tel-Aviv University, Ramat-Aviv, Tel-Aviv 69978, Israel.

[4] School of Earth and Space Sciences, Peking University, China.

[5] California Institute of Technology, Pasadena, CA 91109, USA.

*Correspondence to: christopher.milliner@jpl.nasa.gov

This article has been accepted for publication and undergone full peer review but has not been through the copyediting, typesetting, pagination and proofreading process which may lead to differences between this version and the Version of Record. Please cite this article as doi: 10.1029/2019JB018928

Key Points:

- The mainshock shows almost no shallow slip deficit, with postseismic cGPS showing minor moment release from early, shallow afterslip.
- Afterslip within the first day is consistent with steady-state velocity strengthening friction showing no delayed nucleation or acceleration
- Afterslip and aftershocks show a close correlation within the first hours following rupture, indicating a possible triggering mechanism.

Abstract

Continuous measurements of postseismic surface deformation provide insight into variations of the frictional strength of faults and the rheology of the lower crust and upper mantle as stresses following rupture are dissipated. However, due to the difficulty of capturing the earliest phase of afterslip, most analyses have focused on understanding postseismic processes over timescales of weeks-to-years. Here we investigate the kinematics, moment release and frictional properties of the earliest phase of afterslip within the first hours following the 2016 M_w 7.1 Kumamoto earthquake using a network of five-minute sampled continuous GPS stations. Using independent component analysis to filter the GPS data we find that (1) early afterslip contributes only ~1% of total moment release within the first hour, and 8% after 24 hours. This suggests that the slip model of the mainshock, which we estimate using standard geodetic datasets (e.g., InSAR, GPS and pixel offsets), and which span the first four days of the postseismic period, is largely reflective of the dynamic rupture process and we can rule out contamination of moment release by early afterslip. (2) Early afterslip shows no evidence of a delayed nucleation or acceleration phase, where instead fault patches transition to immediate

deceleration following rupture that is consistent with frictional relaxation under steady-state conditions with dependence only on the sliding velocity. (3) There is a close correlation between the near-field aftershocks and afterslip within the first hours following rupture, suggesting afterslip may still be an important possible triggering mechanism during the earliest postseismic period.

1. Introduction

Analysis from a number of geodetic slip models of large-magnitude continental strike-slip earthquakes have suggested a systematic decrease of coseismic slip in the shallow crust (< 5 km) compared to that at seismogenic depths (~6-10 km), termed the shallow slip deficit (SSD) (Fialko et al., 2005). Numerous mechanisms have been invoked to explain how the rupture may be impeded in the near-surface to produce such slip deficits, including a higher coefficient of fault friction in the shallow crust (Byerlee, 1978), the shallow fault surface having a velocity strengthening frictional rheology (Marone, 1998), interseismic distributed creep or bulk inelastic yielding of the shallow fault-zone that continuously relieves the stored elastic strain (Lindsey et al. 2014), compliant shallow fault zones (Barbot et al., 2008), or dissipation of the rupture energy in the near-surface due to the generation of plastic strain promoted by lower normal stresses (Fielding et al., 2009; Kaneko and Fialko, 2011; Brooks et al. 2017). Knowing how efficiently coseismic ruptures propagate into the near-surface has important implications for accurately simulating the rupture process and generating realistic strong ground motions that affect seismic hazard estimates (Pitarka et al., 2009; Somerville, 2003), as well as how any remnant elastic strain in the shallow crust following a rupture is released throughout the earthquake cycle.

A key remaining issue in accurately characterizing the extent of coseismic shallow slip deficits, is that most geodetically constrained slip models contain an unknown amount of postseismic afterslip. Most geodetic imaging data (e.g., InSAR) are acquired within the first days-to-weeks following rupture which makes it challenging to constrain how contaminated current fault slip models are and how biased estimates of the SSD could be from early and possibly rapid afterslip. Recently proposed dual-inversion approaches that jointly solve for both the co- and post-seismic slip with datasets spanning mixed time periods show promise in addressing this issue in the future, but require availability of continuous and high-density datasets and are limited by possible trade-offs (Liu & Xu, 2019; Ragon et al., 2019). Instances where rapid shallow afterslip could be observed include, the 2014 M_w 6.0 Napa earthquake (Lienkaemper et al., 2016) and the 2004 M_w 6.0 Parkfield earthquake (Freed, 2007), where measurements were acquired early enough to separate early afterslip from coseismic slip in the shallow crust. For the former, 30-40 cm of surface afterslip was measured after ~2 months, which exceeded the coseismic surface slip of ~10 cm, indicating early postseismic slip can contribute a significant amount to shallow fault slip. Therefore, key questions remain as to what is the contribution of early aseismic afterslip in geodetically constrained slip models and how biased are estimates of shallow slip deficits? Constraining the earliest phase of postseismic relaxation, when rates of aseismic moment release are highest, is therefore necessary to better separate between co- and post-seismic moment release and therefore gain a better understanding of the near-surface pattern of strain accumulation and release.

The lack of observational constraints of the early afterslip process (in the hours following rupture), also means the frictional process governing this period is not fully understood. The phenomenological rate-and-state law derived from lab-rock experiments describes how the frictional strength of a fault surface changes as a function of the sliding velocity and state of the surface (Marone, 1998). In the case when the frictional resistance of

the fault surface decreases (increases) this leads to unstable (stable) sliding, termed velocity weakening (strengthening) behavior. However, it is not clear how the velocity strengthening sections on natural fault surfaces may respond to stress perturbations in the hours immediately following rupture and whether the relaxation process initially follows a steady or non-steady state regime. Theoretical rate-and-state predictions of afterslip indicate that the difference between a steady and non-steady state behavior can be distinguished by the differences in slip velocity expected within the first few hours following rupture (Perfettini and Avouac, 2007; Perfettini and Ampuero, 2008). Following a stress perturbation imposed by the main rupture, a velocity strengthening patch under steady-state conditions would experience immediate deceleration with the fault strength depending only on the sliding velocity and not also on the state of the surface (i.e., a velocity-strengthening law). While if relaxation initially occurs under non-steady state conditions the fault patch would experience a transient phase of nucleation and acceleration in the first few hours following rupture and exhibit a frictional dependence on both the state and rate variables (i.e., a full rate-and-state law). Therefore, to separate between these two possible frictional behaviors that governs the conditions by which fault patches relax, it is necessary to capture the kinematics of the earliest phase of afterslip. Analysis of high-rate GPS data revealed ~1.2 hours following the 2003 M_w 8.0 Tokachi-oki earthquake a possible nucleation and acceleration phase, that was consistent with a sliding behavior dependent upon both the velocity and state of the surface (i.e., non-steady state relaxation) (Fukuda et al., 2009). However, the acceleration phase also coincided with a large aftershock and the interpretation is arguably ambiguous as to whether the sudden change in afterslip rate was due primarily to a delayed response following the main rupture associated with a non-steady state nucleation phase, or simply due to a triggered aftershock (Miyazaki and Larson, 2008). An overall lack of observational constraints of the earliest postseismic period makes it difficult to discern whether the frictional process governing afterslip follows a steady-state velocity strengthening behavior

or a non-steady state relaxation, limiting our understanding of the frictional conditions that describe aseismic creep.

The number of aftershocks following the mainshock are well-known to follow an Omori-like, inverse time decay (Utsu et al., 1995), but there is debate concerning the mechanism(s) behind the aftershock production rate. Numerous studies have found a close correlation between afterslip and the cumulative number of aftershocks (e.g., Frank et al., 2017; Gualandi et al., 2014; Lange et al., 2014; Perfettini and Avouac, 2007), and suggested that afterslip may cause stress changes on locked patches of the fault surface that then triggers aftershocks. Other possible mechanisms include dynamic (Gomberg and Johnson, 2005), or static stress changes from the main rupture, that causes aftershocks on a population of sources (Dieterich, 1994; Toda et al., 2012). Although, there is evidence that near-field aftershocks and afterslip correlate strongly over timescales from days to years following the mainshock, there is still no observational constraints as to whether the afterslip-aftershock relation still holds in the earliest stages following rupture and whether afterslip is still a viable triggering mechanism. To answer these questions, we aim to resolve the kinematics of the earliest afterslip in the first minutes to hours following the 2016 M_w 7.1 Kumamoto earthquake using a network of continuous and relatively high-rate (five-minute sampled) GPS positioning (figure 1). From these observations we seek to test the following questions, (i) Is there significant early and rapid afterslip exist that could bias estimates of shallow coseismic slip deficits derived from geodetic slip models (e.g., figure 2)? (ii) What is the frictional process governing the early postseismic phase? and (iii) Does the afterslip-aftershock relation also hold in the hours following rupture?

The 2016 M_w 7.1 Kumamoto earthquake occurred within a dense network of Japan's continuous GNSS stations (GEONet) (Sagiya et al., 2010), and provides a unique opportunity to capture the temporal evolution of early afterslip within the first minutes

following the mainshock rupture. In our analysis we first derive a mainshock slip model for the oblique strike-slip rupture that is estimated from jointly inverting ascending and descending InSAR, GPS, and radar pixel offsets that bracket the mainshock, and like most geodetically constrained slip models contains a component of early postseismic deformation. To then reliably detect the early afterslip signal from the noisy five-minute sampled GPS data we use independent component analysis (ICA), a spatiotemporal filtering technique to extract the dissipating tectonic signal (Hyvärinen and Oja, 2000). An advantage of the ICA approach is that it can separate the afterslip signal from systematic and local noise sources on the basis of statistical independence, obviating a need to impose an assumed functional form as to how the GPS velocities and the inverted afterslip should evolve (such as a log-time or exponential model). We then invert the filtered GPS time series to generate an 'early' afterslip model (spanning the first six days following rupture), constrained using five-minute sampled GPS positioning, and a 'longer-term' afterslip model derived from daily GPS positioning over the first two years (Kositsky and Avouac, 2010). From the 'early' and 'longer-term' afterslip models we can assess the contribution of afterslip to moment release in the shallow crust and the extent to which it may contaminate the geodetically constrained mainshock slip model and estimates of any possible coseismic slip deficits. Using the early afterslip model over the first six days, we then attempt to distinguish what frictional regime (steady or non-steady state) is compatible with the temporal evolution of afterslip. Finally, comparing the evolution of nearfield aftershocks, derived from a template-matching catalogue, to early afterslip from our GPS inversion, we can then assess whether the afterslip-aftershock relation, that has been widely observed at daily-annual timescales, still holds within the hours following rupture.

1.2 Tectonic setting

The 2016 M_w 7.1 Kumamoto earthquake ruptured along the Median Tectonic Line, a

major NE-trending fault system that is part of a transtensional backarc setting accommodating oblique Eurasian-Philippine collision (Figure 1), (Ikeda et al., 2009). The 2016 M_w 7.1 event involved two main fault segments, the NNE-striking Hinagu fault which ruptured for ~10 km, which was the site of rupture initiation and also hosted one of two $M_w \geq 6$ foreshocks, and the NE-striking Futugawa fault to the northeast, that ruptured for ~25 km and where the rupture terminated within the Aso volcano (Shirahama et al., 2016).

Analysis of postseismic deformation following the 2016 Kumamoto earthquake has focused on resolving the deep viscoelastic relaxation response of the lower crust and upper mantle. Moore et al. (2017) developed Green's functions to invert crustal strain rates to estimate the transient lower-crustal rheology below 20 km depth, finding effective viscosities as low as 5×10^{16} Pa.s near the Aso volcano. Similar low transient viscosities of ~10^{17} Pa.s were also found by Pollitz et al. (2017) below 20 km along the central graben system through Kyushu island, which suggested a fluid-rich mantle wedge above the Nankai trough. Compared to these longer-term and deeper crustal studies of postseismic relaxation, here we focus on understanding the aseismic afterslip process within the shallow crust (top 10 km) and first few hours following rupture.

2. Data

To determine the coseismic and postseismic slip distributions we used a range of geodetic data including SAR offsets, InSAR, and continuous GPS, (figure 3).

2.1 InSAR

To measure the far-field coseismic surface deformation, we processed Sentinel-1 ascending (Track 156) and descending (Track 163) pairs acquired in Terrain Observation by Progressive Scan (TOPS) mode following standard two-pass interferometry procedures. The preseismic and postseismic images were acquired on 8 April and 20 April 2016, respectively (Tabls S1). To remove the topographic phase from the SAR images we used a 1-arcsecond SRTM (Shuttle Radar Topography Mission) DEM, and unwrapped the images using the Statistical-Cost Network-Flow Algorithm for Phase Unwrapping (SNAPHU) algorithm (Chen and Zebker, 2001). The unwrapped phase was then downsampled using a quadtree algorithm (figure 3 a, b). Near-field displacements were estimated using split-bandwidth interferometry along the range direction and burst-overlap interferometry along the azimuth direction, respectively following the method of Jiang et al. (2017) (Figure 3 g, h). We also processed a single descending ALOS-2 interferogram that spanned the M_w 6.0 and M_w 6.2 foreshocks (Fig. S1 and Table S1), that occurred ~19 and ~15 hours before the mainshock, respectively, which we inverted to estimate a foreshock slip model and correct for its effect in the geodetic data that brackets the M_w 7.1 mainshock.

2.2 3D near-field measurements

To measure the near-field coseismic surface deformation in areas where the unwrapped radar phase decorrelates as a result of large surface changes (figure 3 d-f), we used cross-correlation of ALOS-2 SAR data in both the range and azimuth directions (Liang and Fielding, 2017). Deriving offsets in the range and azimuth direction from a total of three image pairs (two from descending and one from ascending tracks, see Table S1), provides six unique look directions of surface deformation at decimeter-level precision and ~25 m ground resolution. From the six look directions we solved for the three-dimensional surface motions (east u_e, north

u_n and up u_u), using a weighted least-squares approach (see eq. 1 and 2, and Figure 3 d-f for results, Fialko et al., 2001).

$$\boldsymbol{P} = \begin{bmatrix} p_{azi}^{desc-l} \\ p_{R}^{desc-l} \\ p_{azi}^{desc-r} \\ p_{R}^{desc-r} \\ p_{azi}^{asc-r} \\ p_{R}^{asc-r} \end{bmatrix} \quad (1)$$

$$[u_e\ u_n\ u_u\ ] = (P^T \Sigma_d P)^{-1} P^T d \quad (2)$$

Where p is the unit vector representing surface motion projected into the range (R) or along-track (azi) direction, where the superscript in eq. (1) denotes whether the satellite was in an ascending (asc) or descending (desc) orbit and looking left (l) or right (r). The diagonal components of the weighting matrix (Σ_d) includes the inverse of the variance estimated from a far-field stable region, and d is the data vector containing the offset values. From the 3D deformation maps we then extracted the horizontal and vertical fault slip offsets along the surface rupture using stacked profiles oriented perpendicular to the fault traces, which produces the along-strike surface slip distribution (Figure 3i). These offset measurements provide an estimate of the total surface displacement across the entire rupture-zone width (i.e., both the on and off-fault deformation), by extrapolating the surface motion from either side of the fault zone towards the primary fault trace (e.g., Rockwell et al., 2002; Milliner et al., 2015). The surface slip distribution shows a slightly asymmetric elliptical shape with a sample mean displacement of 2.36 ± 0.4 m (standard error), and a maximum of 2.86 ± 0.67 (1σ) m located northeast of the Hinagu-Futugawa fault intersection, and have good agreement with offsets estimated from 2D subpixel correlation of a pair of Sentinel-2 optical images processed using COSI-Corr (Figure S2) (Leprince et al., 2007). These near-field ALOS-2 offset measurements

help constrain fault slip in the top cells of the slip model and are therefore complementary to the other geodetic observations used here (e.g., InSAR and GPS,), which constrain the far-field elastic response of the crust due to deeper slip.

2.3 GPS

For both the coseismic and postseismic slip models we used 63 continuous GPS stations. For the early phase of afterslip (during the first six days), we used the five-minute sampled time series, and to study the longer-term postseismic process (the following two-years) we used the daily sampled product. The GPS time series were obtained from the Univ. of Nevada Reno geodetic lab (http://geodesy.unr.edu/), (Blewitt et al., 2018), which processes the time series in precise point positioning mode using GIPSY/OASIS-II version 6.1.1. The time series are aligned to the IGS08 reference frame, and have been corrected for diurnal, semidiurnal, M_f, and M_m ocean tide loading using the tidal model FES04, while the semi-annual tidal loading as well as the solid Earth tide and pole tide have been corrected following the IERS (International Earth Rotation and Reference Systems Service) 2010 conventions (Petit and Luzum, 2010). The Earth Orientation Parameters of the model have been calculated using the IERS 2010 conventions for diurnal, semi-diurnal, and long period tidal effects. To estimate the coseismic offset at each station we used the five-minute sampled time series, and removed a pre-earthquake velocity using positions six days prior to the mainshock and then simply differenced the average position in all three components from one hour before and after the event (figure 3c). For the postseismic GPS analysis we describe in the next section the use of a spatio-temporal filtering technique to help extract the time-varying afterslip signal and to improve the signal-to-noise ratio.

3. Methods

3.1 Spatiotemporal filtering using Independent Component Analysis (ICA)

One of the major noise sources in the analysis of regional GPS networks is common-mode error (CME). This systematic noise source is thought to arise from a combination of uncertainties in GPS orbital position, reference frame and large-scale atmospheric modeling (Dong et al., 2006; Serpelloni et al., 2013; Wdowinski et al., 1997; Williams Simon D. P. et al., 2004). To isolate and separate the tectonic signal from systematic noise sources such as CME, we use a spatiotemporal filtering technique called ICA (Le et al., 2011). ICA is a form of blind source separation that seeks to separate a set of latent variables under the assumption that they are statistically independent (see section S1 for more details on the ICA method). Here, we have used the reconstruction ICA approach (Le et al., 2011) to estimate the unknown sources, which differs from other ICA methods, such as fastICA (Hyvärinen and Oja, 2000), by swapping the orthonormality constraint applied to the un-mixing matrix, with a reconstruction penalty term added explicitly to the objective function, which gives the benefit of using unconstrained solvers (see equation 2 of Le et al. (2011), and section S1 and eq. S1 here). The ICA approach allows for a variable spatial weight for each station and source, allowing ICA to account for correlated, spatially varying CME across the network (Dong et al., 2006), which is advantageous over typical network filtering techniques such as regional stacking, which assumes regional stacking is a uniform effect (Wdowinski et al., 1997). To determine the number of components to decompose the data into, we used North's rule of thumb (North et al., 1982), a stopping-rule approach that helps define the statistical significance of each component relative to its uncertainty (see section S2 for additional details). For the

five-minute GPS data, we found that four components were significant, and for the daily GPS data, five components (Figure S7).

The ICA filtering is applied separately to the five-minute and daily GPS time series, giving independent constraints of the early and later phases of postseismic surface deformation. For the five-minute time series we were not able to include the vertical component, as we could not resolve a robust tectonic signal due to the large noise. However, for the daily longer-term time series we were able to use all three-components of motion. From the ICA decomposition of the five-minute sampled, early postseismic GPS data (figure 4), we interpret the first and second ICs as representing CME due to the uniform spatial response, incoherent temporal pattern and the largest contribution to variance (eq. S2). We interpret the fourth IC as the tectonic signal (figure 4), as it exhibits a temporal component with a clear log-like time decay and a spatial response that is consistent with fault-related shear motion across the north-east trending Kumamoto rupture. Projecting the data onto this single component reduces the WRMS by 91% (the median value estimated from all stations). We suspect that the third component is related to either volcanic and/or non-tidal ocean loading (or both) due to the large spatial responses in proximity to the active volcanoes (black triangles in Figure 4d) and coastal regions. For the longer-term postseismic, daily time series, we find that the second, third and fourth ICs reflect periodic signals and CME, while the tectonic signal is represented by the first IC (Figure S4). Selecting only the first IC reduces the WRMS of the time series on average by 47%, a smaller decrease than that found from the five-minute data because the long-term postseismic signal still contributes a relatively larger amount of the total variance of motion across the network.

In postseismic studies that use daily sampled GPS positioning, typically the first postseismic day is defined as the reference epoch from which future changes in position are measured from. However, this step removes any post-seismic motion that may have accrued

within the first day following rupture, which can contribute a significant amount of displacement (Hill et al., 2012; Twardzik et al., 2019). Here, as we can measure the total displacement of each station within the first 24 hours after the earthquake using the higher rate (5-minute) sampled positioning (figure 6), we correct the daily postseismic GPS positions to include this amount by taking the average amount of displacement measured within the first 24 hours (of the first postseismic UTC day, which is ~8 hours after the event and includes motion up to this time). This increases the daily GPS displacement by up to 14 mm for some near-field stations (Fig. S20).

3.2 Inversion of Geodetic Data for fault slip

To estimate the coseismic slip distribution we invert the geodetic data (Fig. 3), using a weighted non-negative least-squares method assuming a homogenous elastic half-space (Okada et al., 1992), and apply a finite-difference gradient smoothing regularization to the solution. The time-varying postseismic slip is estimated using an inversion approach similar to the independent component analysis-based inversion method (ICAIM) (Kositsky and Avouac, 2010), using only the GPS time series, and where we deepen, lengthen and coarsen the fault segments. To estimate the fit of both the co- and postseismic models to the data and variations in the degree of smoothing we use the percent of variance reduction (POVR) (see eq. S3, and section S7 and for more details of the inversion approach and fault parameterization).

4. Results

The mainshock slip model is able to fit the geodetic data well, with POVR values of 91% for the GPS, 97% for the ALOS-2 radar fault offsets, 89% for the Sentinel-1A azimuthal offsets, 93% for the Sentinel-1 range offsets, 63% for the descending InSAR, and 86% for the ascending InSAR (see Figure S3 for fits and residuals). The relatively poor model fit to the

descending InSAR data is likely the result of the inability of the elastic model to reproduce the complex non-tectonic deformation within the Aso caldera that resulted from lateral spreads and shaking-induced slumping, where we find the largest misfits (Fig. S3), (Tajima et al., 2017; Tsuji et al., 2017).

The mainshock slip model indicates a total seismic moment of 3.86×10^{19} N·m, that is equivalent to a moment magnitude of M_w = 7.06 (assuming a shear modulus of 30 GPa), that is close to the seismologic estimate from strong ground motion inversion of M_w = 7.06 (3.9×10^{19} N·m) Hao et al. (2016), and the USGS GCMT of M_w = 7.0. Largest slip of 5.48 ± 0.3 m is found along the Futugawa fault at ~9 km depth that decreases sharply along-strike to zero towards the Aso volcano, a feature common amongst other coseismic models derived from geodetic and seismologic data (Asano and Iwata, 2016; Yagi et al., 2016; Kobayashi et al., 2017; Scott et al., 2019), and large shallow slip along the south-west end of the Futugawa fault (2-3 m), also consistent with previous slip models (see Figure S14).

4.1 Early postseismic afterslip

To resolve the kinematics and moment release of the earliest phase of afterslip in the first hours following rupture we inverted the filtered GPS five-minute sampled time series over the first six days. The kinematic afterslip model shows a reasonably good fit to the GPS time series, with POVR of 85% and 88% for the east, and north components, respectively. The afterslip moment decays almost in a log-time fashion, as illustrated in figure 7c. After the first hour the total cumulative aseismic moment amounts to 3×10^{17} N·m (M_w = 5.7), which is ~1% of seismologic coseismic moment, and after 24 hours is 3×10^{18} N·m (M_w = 6.3), or 8% of the coseismic moment release (Hao et al., 2016). Within the top 5 km of the crust we find that the moment release from afterslip is almost half of the total aseismic moment (or 4% of the

coseismic amount), with only 1.5×10^{17} N·m released within the first hour and 1.5×10^{18} N·m after 24 hours. Afterslip on the Futugawa fault is almost zero within the main area of large coseismic slip at ~10 km depth, suggesting our afterslip model can resolve the first-order features of the slip distribution (see also figure S10 for model uncertainty estimates).

4.2 Longer term afterslip

To constrain the longer-term moment release from afterslip and its contribution to compensating for deficits in shallow coseismic slip, we inverted the daily ICA filtered GPS time series over the first two years following the mainshock. Aseismic moment release again exhibits a log decay with time, where after two years we find a total aseismic moment of 1.2×10^{19} N·m, that is ~30% of the seismologically estimated moment (Asano and Iwata, 2016), and within the top 5 km of the crust an aseismic moment of 5.1×10^{18} N·m, or ~13% compared to the coseismic amount. Within regions of the model space that we can resolve well (< 20 km depth, Figure S10) the spatial distribution of longer-term afterslip shows a similar spatial pattern to the early afterslip (Figure 7). Over the first two years there is again a noticeable lack of afterslip within the main coseismic asperity patch on the Futugawa fault and immediately below the Aso volcano at depth (< 20 km).

4.3 Deficits of Shallow Co- and Postseismic Slip

To characterize how co- and post-seismic slip varies as a function of depth and any possible shallow slip deficits, we integrate the norm of the slip vector along-strike for each depth layer and normalize by the largest value (Figure 5b). This is calculated across both the Hinagu and Futugawa faults, giving the average slip-depth distribution across the entire rupture

plane. The SSD value is then estimated from the normalized slip-depth function in Figure 5b as, $[1 - (S_s/S_{max})]\cdot 100$, where S_s is the integrated surface slip value and S_{max} is the maximum integrated slip at any depth. The slip-depth distribution from the mainshock model (which includes early afterslip, figure 5) exhibits almost no deficit, at 2 ± 3%, indicating that the overall surface slip across the rupture plane is similar to that at depth (Figure 5b). However, in local areas of the rupture the slip-depth distribution can be found to significantly deviate from this rupture-average slip deficit. For example, along the mid-section of the Futugawa fault where the main slip asperity is located, there is locally a large SSD of 33 ± 6%. Whereas further to the southwest along the Futugawa fault there is interestingly a site of higher slip at the surface (1.87 m) than that at depth (1.1 m) producing a negative SSD (-50 ± 8%), which we term a shallow slip surfeit (SSS). This surfeit can explain why the rupture-averaged SSD is close to zero and that the overall slip is balanced across the rupture plane. We note that other slip models estimated using different datasets (strong ground motion data and InSAR), show a similar SSS along the southwest end of the Futugawa fault (see Figure S14), (Asano and Iwata, 2016; Jiang et al., 2017; Kobayashi et al., 2017; Yagi et al., 2016).

Reliable estimates of the slip-depth distribution require near-field geodetic observations of surface deformation to help constrain slip at shallow depths (< 5 km) (Xu et al., 2016) as well as consideration of the effects of the spatial smoothing associated with regularization of the solution. Here we incorporate 3D ALOS-2 SAR offsets and Sentinel-1 range offset data into the inversion that we find provides reasonable constraints for shallow slip as found by low model uncertainty estimates of < 15 cm (figure S9) and high model resolution values of > 0.9 at depths < 5 km (Figure S8, Du et al., 1992). To mitigate the effects of spatial smoothing, which can problematically flatten the slip-depth distribution and underestimate the slip deficit, we use a similar approach of Xu et al. (2016) where a minimal smoothing factor is chosen that corresponds to the start of the decrease in model fit measured using the POVR (Fig. S17). This

approach is advantageous over a typical L-curve method as the optimal trade-off location (point of maximum curvature) between the model misfit and roughness is arbitrarily dependent upon the range of values chosen (Hreinsdottir et al., 2002).

4.4 Frictional analysis

To constrain the frictional behavior of the fault surface undergoing afterslip (i.e., *a*-*b*, which controls the instantaneous (*a*) and the steady-state velocity-dependence of friction (*b*)) we use a simple velocity-strengthening friction sliding law (Marone, 1998; Dieterich, 2007). The velocity strengthening law models the evolution of afterslip as a zero-dimensional spring-block slider system responding to an imposed stress change, with dependence only on the rate and not on the state variable, an assumption that we discuss and justify later in section 5.3 where we find that the kinematics of the observed afterslip are inconsistent with a full rate-and-state law. The frictional parameters (*a*-*b*) are estimated by fitting the time evolution of afterslip, δ(t), of the velocity strengthening model shown in eq. (3) to model fault patches that experience an increase of Coulomb stress. The velocity strengthening law models the evolution of afterslip relative to a reference epoch (t_1), chosen here as the first sample five-minutes after the mainshock (following Gualandi et al., 2014),

$$\delta(t) - \delta(t_1) \approx \alpha \, In\left(\frac{\alpha + \beta t}{\alpha + \beta t_1}\right) \tag{3}$$

with the assumption that the period of observation *t* is smaller than the characteristic decay time ($t_d = \alpha / V_{pl}$), where V_{pl} = loading plate velocity. From Marone et al. (1991), $\alpha = (a\text{-}b)\,\sigma/k$ and β is the starting sliding velocity on the patch at the onset of postseismic slip ($t \approx 0$), σ the effective normal stress on the fault surface and *k* is the spring stiffness representing the

rigidity of the host rock. We assume an effective normal stress (lithostatic-hydrostatic pressure, with density of 2700 and 1000 kg/m^3, respectively), k = 30 GPa, and $V_{pl,}$ = 2 mm/yr derived from paleoseismic analysis of the Futugawa fault (Lin et al., 2017). From eq. (3) we estimate α and β for the early phase of afterslip from each fault patch using a non-linear inversion method, finding values from 0.1-1.5 cm and 0.1-2.5 cm/hour, respectively. This indicates a t_d of ~5.6 years, which is significantly larger than the GPS observation period of six days, indicating that the condition $t << t_d$ in eq. (3) is satisfied. Coulomb stress changes (ΔCFF) are then calculated for each afterslip patch using the stress changes due to the mainshock slip model (figure 5), and assuming a static frictional coefficient of μ_s = 0.4. Using the estimate of β derived from the early phase of afterslip and eq. 4 we find a-b values along the Hinagu and Futugawa faults ranging from 10^{-4}-10^{-2} (Figure 8). We do not apply the frictional analysis to afterslip estimated over the longer-term (two years), because this later phase of deformation is increasingly affected by viscoelastic relaxation which we do not formally correct for.

$$a - b = \frac{\Delta CFF}{\sigma \cdot log\left(\frac{\beta}{V_{pl}}\right)} \quad (4)$$

Estimates of β also provide constraint for the time of maximum slip velocity (Perfettini & Ampuero, 2008), which we find ranges from ~3 hours-140 days, indicating the temporal sampling of the GPS data (5-minutes) and period of observation (up to 2 years) should be sufficient to resolve the possible occurrence of a transient phase of acceleration (see section S6 for details).

5. Discussion

5.1 Shallow slip deficits

A remaining problem in understanding the true extent of the shallow slip deficits for large magnitude earthquakes, is the extent of contamination of geodetically constrained slip models by early and possibly rapid afterslip. Such mixing of co- and early postseismic slip in finite-fault models is problematic as it would bias our understanding of the rupture kinematics, such as how well the rupture propagates through the near-surface and how the accumulated elastic strain in the shallow crust that may not be fully released coseismically, is relieved later on in the earthquake cycle (assuming strain is conserved with depth over time). Inversion of the five-minute sampled GPS positioning reveals that the slip-depth distribution of early afterslip resolved after the first day shows it is mostly concentrated in the upper 5 km of the crust (Figure 7a). The largest concentration of early afterslip (up to 15 cm) occurs near the Hinagu and Futugawa fault intersection and along the Futugawa fault, with smaller amounts above and northeast of the large main slip patch, which is consistent with aseismic slip acting to relax strains imposed in the shallow crust. Importantly this shows in this case that even in regions where there are large local coseismic slip deficits, early and rapid afterslip does not compensate significantly for such coseismic deficits in the shallow crust. Overall, the total early afterslip after the first hour following rupture, amounts to only ~1% of moment release by the mainshock, and 8% by the end of the first day, with 4% released in the upper 5 km of the crust (where the coseismic moment is constrained from seismology and independent of aseismic afterslip), and maximum postseismic slip of ~24 $\pm$ 8 cm. This indicates that for the Kumamoto earthquake, rapid and early afterslip does not contribute a significant amount of slip in the shallow crust. In addition, it suggests that the balanced slip-depth distribution from the mainshock slip model (an SSD of almost zero), is largely reflective of the dynamic rupture process. The relatively low amount of afterslip for this event may indicate that relatively larger shallow afterslip found in other earthquakes (e.g., the 2014 Napa and 2004 Parkfield

earthquakes), may only pertain to smaller magnitude events ($M_w < 6.5$), which are ruptures that fail to completely propagate through the surface. This behavior was noted by Fattahi et al. (2015), that found from a compilation of 22 events, that more moderate earthquakes ($M_w < 6$) have a larger relative amount of shallow postseismic slip than coseismic. A possible reason for this difference in behavior is that smaller events typically occur on less structurally well-developed faults with a rougher geometry, or the effects of velocity strengthening friction in the shallow crust, which can both inhibit efficient rupture within the near-surface and lead to incomplete stress drops (Ma, 2008).

To understand whether the near-zero slip deficit we find is a robust feature we compare it against estimates from other slip models of the Kumamoto earthquake inverted using different datasets and inversion strategies (figure 5b) (Asano and Iwata, 2016; Yagi et al., 2016; Kobayashi et al., 2017; Scott et al., 2019). Although there is a range of behaviors for how coseismic slip varies with depth, most indicate slip at the surface is similar to that at seismogenic depths (6-8 km), with SSD values ranging from 1-15%. The model with the largest slip deficit of ~15% is that of Scott et al. (2019), which uses similar geodetic data as that used here (including Sentinel-1 InSAR to constrain far-field deformation and near-field constraints from optical image correlation and lidar data). However, two differences between these studies is that here we have incorporated 3D near-field offsets along the entire length of the surface rupture (~35 km) as opposed to only ~14 km constrained by the lidar data, and the other is the manner in which the near-field data are inverted. Regarding the latter, instead of inverting the measurements of surface motion directly (e.g., Fig. 3 d-f), which would assume all near-field motion is elastic, we have instead inverted the fault offsets (Fig. 3i), which approximates the full fault-zone 'displacement' as being a combination of the discrete (traditional on-fault displacement) and distributed fault-parallel inelastic shear, the latter which cannot be modeled elastically (Gold et al., 2015; Milliner et al., 2015; Fujiwara et al., 2016; Shirahama et al., 2016;

Toda et al., 2016). This explicitly constrains the top cells of the model using the total across-fault inelastic 'strain' (e.g., Xu et al. 2016), which includes the distributed component of inelastic shear strain that is known from geologic and geodetic observations to accommodate a significant portion (up to 40%) of the total coseismic fault strain (Rockwell et al. 2002; Dolan & Haravitch, 2014; Zinke et al., 2014; Gold et al. 2015; Milliner et al. 2015, 2016; Teran et al. 2015; Scott et al., 2018). We note that the 15% SSD value reported here for the Scott et al. (2019) study differs from their reported value as we have found their approach to calculate the slip-deficit (which uses the median value for each depth interval) leads to a slight underestimation of shallow slip (see supplements section S3 for more details), and is a different approach to that used by previous work and here (which integrates the total slip for each depth interval, e.g., Fialko et al., 2005; Xu et al., 2016). Although, there are differences in the extent of the SSD and slip-depth functions between the various slip models (figure 5b), such variation is useful in characterizing the epistemic uncertainty of the slip-depth distribution and SSD estimates, which arises from the use of different parameterizations, types of regularization (here we minimize the gradient, while others use a curvature penalty), strength of smoothing, data weighting, and data types. The first-order agreement of the slip-depth functions between the various slip models (Figure 5b), and the use of 3D near-field data here to constrain shallow slip, gives us confidence that the coseismic shallow slip of the Kumamoto earthquake is likely similar to that at seismogenic depths. In addition, as our postseismic GPS analysis indicates there is minimal contamination from early afterslip, this supports the notion that the balanced slip distribution found from the mainshock model (i.e., lack of shallow slip deficit), can be regarded as a feature reflective of the dynamic rupture process (e.g., Fig. 2b).

Decomposing the overall 'oblique' slip-depth distribution, which has almost no deficit (~2%, Fig. 5b), into the dip-slip and strike-slip components shows a prominent surfeit and minor deficit (~10%), respectively (Fig S22). If it is assumed that over multiple earthquake

cycles strain release is conserved with depth, these large differences in the co-seismic slip-depth distributions raise the question as to how it is accommodated over the longer-term? Specifically, what is not understood is whether these coseismic slip surfeits and deficits are a persistent feature, or if the slip vector may change considerably from event-to-event that may eradicate slip deficits from prior events and conserve the long-term slip budget. Evidence of considerable variation in the slip vector from event-to-event has been found (by up to almost 90^{o}) from geologic observations of slickenlines, fibre lineations and gouge fabrics from other fault systems (e.g., the Makran fault system, Platt et al., 1988). On the other hand, if the coseismic slip-depth distributions are persistent and reflective of the longer-term strain release, this would suggest that the depth distribution of interseismic release of elastic strain (e.g., via distributed bulk inelastic yielding), must be different in order to conserve the long-term slip budget with depth. Understanding the persistence or lack thereof, of slip deficits and surfeits from event-to-event has important implications for understanding the evolution of strain and stress in the crust, interpreting the incomplete record of paleo-earthquake slip, and realistic dynamic rupture simulations and calculations of seismic shaking for accurately characterizing the hazard.

We note that another possible mechanism to explain the lack of a slip deficit for this rupture is the presence of the Aso volcano at the north-east termination of the rupture. This is a region of elevated crustal temperatures which would inhibit slip at depth and limit slip to the shallow surface. This would produce a pronounced shallow slip surfeit in this region which would act to lower the overall slip deficit when considering the slip variation along the entire rupture length.

5.2 Aftershock-Afterslip relation

To assess whether a relation exists between the rate of aftershocks and afterslip in the early stages of postseismic relaxation, we compare our early afterslip model to aftershocks from a seismic catalogue from Yue et al. (2017). Such a correlation has been interpreted as the afterslip process influencing the aftershock production, due to afterslip loading unstable patches of the fault surface that then break in aftershocks. To help expand the number of aftershock events we use a seismic catalogue generated using a template matching approach (Ross et al., 2016; Shelly et al., 2016), leading to 35,703 precisely located aftershocks (see Yue et al., 2017 for details). Comparison of the evolution of the cumulative number of aftershocks (using only well-detected events of $M_w > 2$) with early afterslip shows that within the first six days they both follow a similar temporal decay. A similar afterslip-aftershock relation has been observed elsewhere following other large events such as the 1992 Landers, 2009 L'Aquila, 2010 Maule and 2015 Illapel earthquakes (Frank et al., 2017; Gualandi et al., 2014; Lange et al., 2014; Perfettini and Avouac, 2007), but has only been observed in the later stages of the aftershock sequence, at timescales of days-years following the mainshock. Here we show that this relation still holds within the first hours following the main event over the first six days (Figure 7c), suggesting afterslip may still influence and possibly trigger aftershocks even at these early timescales, alongside the effects of dynamic and static Coulomb stresses (Dieterich, 1994; Gomberg and Johnson, 2005).

When comparing the longer-term decay of aftershocks with afterslip (Figure 7d) over the first two years, we find a noticeably weaker correlation. We interpret the afterslip-aftershock discrepancy as the result of an increasing contribution of viscoelastic relaxation to the surface deformation field, that is known to have a larger effect over longer timescales of months-years (Freed et al., 2006) and has not been removed from the daily GPS time series. A prominent viscoelastic response is not surprising given previous postseismic geodetic studies

over the first nine months following the Kumamoto earthquake found transient weak viscosities of 10^{17}-10^{18} Pa·s that are likely related to arc-magmatism (Moore et al., 2017; Pollitz et al., 2017). A prominent viscoelastic response would also explain why the GPS time series exhibits a slower decay rate than the aftershock rate (Figure 7d), and why our afterslip model exhibits a relatively poorer fit to the vertical component of the GPS data than the horizontals (POVR of 67% and 83%, respectively, see Fig. S18). This apparent afterslip-aftershock discrepancy contrasts with other earthquakes, such as following the 2004 Parkfield or 1992 Landers events, which showed a strong correlation over similar timescales of weeks-years that was attributed to afterslip driving aftershock production (Perfettini & Avouac, 2007; Barbot et al., 2009). Here we believe the lack of an apparent correlation highlights the more prominent effect of viscoelastic relaxation occurring in a back-arc extensional setting that could be masking surface strain resulting from afterslip, and is an effect that should be modeled and removed first before it can be determined whether an afterslip-aftershock correlation exists or not.

5.3 Frictional Behavior of Early Afterslip

To determine whether a rate-state or velocity-strengthening frictional regime governs the frictional behavior of the fault surface, where the former predicts a transient phase of slip acceleration following rupture, while the latter expects a continuous deceleration (Perfettini and Avouac, 2007), we attempt to resolve the earliest phase of the afterslip evolution in the minute-to-hours following rupture. From our early afterslip model that constrains the slip evolution at a sampling rate every five minutes, we can detect no transient phase of nucleation and acceleration within the first few days, and instead find an almost continuous deceleration of afterslip following an almost log-time decay. In addition, we find no evidence of accelerated aftershocks rates (Figure 7c), which would otherwise suggest a phase of possible afterslip acceleration (assuming the afterslip-aftershock relation is valid over such a timescale). We note

that the deviation of afterslip at ~14 hours after rupture is likely an artifact as it is similar to deviations seen later in the time series, which would otherwise suggest the fault experiences back-slip that then recovers, which is physically unlikely and not predicted by either the velocity strengthening or rate-state laws. In addition, when estimating the power spectral density of the residuals (where the velocity strengthening prediction is removed from the time series), we find a weak periodicity at ~12 hours (Fig S6), that could indicate these deviations are related to possible hydrologic, thermoelastic or volcanic deformation recorded at GPS stations. Furthermore, when isolating the large deviation at ~14 hours using the ICA approach we find its spatial pattern is inconsistent with a tectonic or afterslip process, and instead find GPS motions are largest around the volcano and orientated in a north-west direction (see supplement S5 for more details).

Finding afterslip exhibits no clear transient phase of acceleration, we assume its evolution can be described by a simple velocity strengthening law, allowing us to estimate the frictional properties of the fault surface from eq. (4), (Gualandi et al., 2014; Marone et al., 1991). This relation models the evolution of afterslip on a velocity strengthening patch as a spring-block slider system, where the *a-b* parameter describes how the frictional resistance of the sliding block changes in response to a velocity strep imposed by the mainshock. From this model we find *a-b* values ranging from 10^{-4}-10^{-2}, with values highest at shallower depths and on the Futugawa fault (Figure 8). Such small a-b values are indicative of a frictional surface that is slightly velocity-strengthening, which under the appropriate loading conditions can undergo either creep or sustain instabilities, termed a compliant field (Boatwright & Cocco, 1996). Such a compliant frictional regime could explain why both aftershocks and afterslip are found to occur along both the Futugawa and Hinagu faults, which is a behavior also found following the 2009 L'Aquila and 2015 Illapel earthquakes (Gualandi et al., 2014; Frank et al., 2017).

6. Conclusions

Using an independent component filtering technique to track the earliest evolution of aseismic moment release, when rates are highest, reveals it amounts to ~1% of the coseismic moment within the first hour (M_w=5.7), and ~4% (M_w=6.1) by the end of the first day (within the top 5 km of the crust). This suggests we can be confident that the balanced slip-depth distribution (i.e., a lack of a shallow slip deficit) found for the mainshock (that is constrained by geodetic data that spans the mainshock and includes early postseimsic slip), is largely reflective of the coseismic rupture process, and has minimal contamination from rapid afterslip. Resolving the early kinematics of the afterslip process also us to understand the frictional regime that governs the afterslip process. Within the first few hours following rupture, afterslip exhibits no evidence of a delayed nucleation and acceleration phase that is predicted by a full rate-and-state behavior, and instead afterslip patches undergo immediate deceleration following rupture that is consistent with a simple velocity-strengthening friction law indicating steady-state relaxation (i.e., no dependence on the state-variable). Lastly, even within the first minutes-to-hours following the rupture there still seems to be a close relation between afterslip and the cumulative number of aftershocks, a behavior that is similar to that found following other earthquakes over longer timescales of months-years, suggesting that afterslip could still influence aftershock production during these early periods.

Acknowledgements

General: We would like to thank Yuri Fialko and one anonymous reviewer for their helpful suggestions. We also thank David Bekaert and Adriano Gualandi for helpful discussions.

Funding: Part of this research was supported by the NASA Earth Surface and Interior focus area and performed at the Jet Propulsion Laboratory, California Institute of Technology. Funding for this project was provided under a NASA Postdoctoral Program fellowship to C. Milliner administered by the Universities Space and Research Association through a contract with NASA, and a NASA ESI grant NNX16AL17G awarded to R. Bürgmann. **Author contributions:** C.M. and R.B. developed the framework of the study. C.M. performed postprocessing of GPS data and developed the inverse scheme. T.W. processed the Sentinel InSAR data, A.I. helped with analysis of seismicity data and C.L. helped processing the ALOS-2 scenes. All authors participated in manuscript revision. **Competing interests:** The authors declare that they have no competing interests. **Data and materials availability:** GPS raw and filtered time series are available as supplementary files and can be downloaded from the online open access data respository site Zenodo (https://doi.org/10.5281/zenodo.3522444)

References

Argus, D.F., Gordon, R.G. (1991). No-net-rotation model of current plate velocities incorporating plate motion model NUVEL-1. Geophys. Res. Lett. 18, 2039–2042. https://doi.org/10.1029/91GL01532

Asano, K., Iwata, T. (2016). Source rupture processes of the foreshock and mainshock in the 2016 Kumamoto earthquake sequence estimated from the kinematic waveform inversion of strong motion data. Earth Planets Space 68, 147. https://doi.org/10.1186/s40623-016-0519-9

Barbot, S., Fialko, Y. and Sandwell, D., 2008. Effect of a compliant fault zone on the inferred earthquake slip distribution. *Journal of Geophysical Research: Solid Earth*, *113*(B6).

Barbot, S., Fialko, Y. (2010). A unified continuum representation of post-seismic relaxation mechanisms: semi-analytic models of afterslip, poroelastic rebound and viscoelastic flow. Geophys. J. Int. 182, 1124–1140. https://doi.org/10.1111/j.1365-246X.2010.04678.x

Biot, M.A. (1956). Theory of Propagation of Elastic Waves in a Fluid-Saturated Porous Solid. II. Higher Frequency Range. J. Acoust. Soc. Am. 28, 179–191. https://doi.org/10.1121/1.1908241

Boatwright, J. & Cocco,M., 1996. Frictional constraints on crustal faulting, J. geophys. Res., 101(B6), 13 895–13 909

Brooks, B.A., Minson, S.E., Glennie, C.L., Nevitt, J.M., Dawson, T., Rubin, R., Ericksen, T.L., Lockner, D., Hudnut, K., Langenheim, V. and Lutz, A. (2017). Buried shallow fault slip from the South Napa earthquake revealed by near-field geodesy. *Science advances*, *3*(7), p.e1700525. doi: 10.1126/sciadv.1700525

Byerlee, J., (1978). Friction of Rocks, in: Byerlee, J.D., Wyss, M. (Eds.), Rock Friction and Earthquake Prediction, Contributions to Current Research in Geophysics (CCRG). Birkhäuser Basel, Basel, pp. 615–626. https://doi.org/10.1007/978-3-0348-7182-2_4

Chen, C.W., Zebker, H.A. (2001). Two-dimensional phase unwrapping with use of statistical models for cost functions in nonlinear optimization. JOSA A 18, 338–351. https://doi.org/10.1364/JOSAA.18.000338

Cohen-Waeber, J., Bürgmann, R., Chaussard, E., Giannico, C. and Ferretti, A. (2018). Spatiotemporal Patterns of Precipitation-Modulated Landslide Deformation From Independent Component Analysis of InSAR Time Series. *Geophysical Research Letters*, *45*(4), pp.1878-1887. https://doi.org/10.1002/2017GL075950

Dieterich, J. (1994). A constitutive law for rate of earthquake production and its application to earthquake clustering. J. Geophys. Res. Solid Earth 99, 2601–2618. https://doi.org/10.1029/93JB02581

Dieterich, J. (2007), Applications of rate- and state-dependent friction to models of fault slip and earthquake occurrence, Treatise on Geophysics, 4, 107-129.

Dolan, J.F. and Haravitch, B.D. (2014). How well do surface slip measurements track slip at depth in large strike-slip earthquakes? The importance of fault structural maturity in controlling on-fault slip versus off-fault surface deformation. Earth and Planetary Science Letters, 388, pp.38-47.

Dong, D., Fang, P., Bock, Y., Webb, F., Prawirodirdjo, L., Kedar, S., Jamason, P. (2006). Spatiotemporal filtering using principal component analysis and Karhunen-Loeve expansion approaches for regional GPS network analysis. J. Geophys. Res. Solid Earth 111, B03405. https://doi.org/10.1029/2005JB003806

Du, Y., Aydin, A., Segall, P. (1992). Comparison of various inversion techniques as applied to the determination of a geophysical deformation model for the 1983 Borah Peak earthquake. Bull. Seismol. Soc. Am. 82, 1840–1866.

Fattahi, H., Amelung, F., Chaussard, E., Wdowinski, S. (2015). Coseismic and postseismic deformation due to the 2007 M5.5 Ghazaband fault earthquake, Balochistan, Pakistan. Geophys. Res. Lett. 42, 3305–3312. https://doi.org/10.1002/2015GL063686

Fialko, Y., Simons, M., & Agnew, D. (2001). The complete (3-D) surface displacement field in the epicentral area of the 1999 Mw7. 1 Hector Mine earthquake, California, from space geodetic observations. *Geophysical research letters*, *28*(16), 3063-3066. https://doi.org/10.1029/2001GL013174

Fialko, Y., Sandwell, D., Simons, M., Rosen, P. (2005). Three-dimensional deformation caused by the Bam, Iran, earthquake and the origin of shallow slip deficit. Nature 435, 295. https://doi.org/10.1038/nature03425

Fielding, E.J., Lundgren, P.R., Bürgmann, R. and Funning, G.J. (2009). Shallow fault-zone dilatancy recovery after the 2003 Bam earthquake in Iran. *Nature*, *458*(7234), p.64. doi: https://doi.org/10.1038/nature07817

Frank, W.B., Poli, P., Perfettini, H. (2017). Mapping the rheology of the Central Chile subduction zone with aftershocks. Geophys. Res. Lett. 44, 5374–5382. https://doi.org/10.1002/2016GL072288

Freed, A.M. (2007). Afterslip (and only afterslip) following the 2004 Parkfield, California, earthquake. Geophys. Res. Lett. 34(6). https://doi.org/10.1029/2006GL029155

Freed, A.M., Bürgmann, R., Calais, E., Freymueller, J., Hreinsdóttir, S. (2006). Implications of deformation following the 2002 Denali, Alaska, earthquake for postseismic

relaxation processes and lithospheric rheology. J. Geophys. Res. 111(B1). https://doi.org/10.1029/2005JB003894

Fujiwara, S., Yarai, H., Kobayashi, T., Morishita, Y., Nakano, T., Miyahara, B., Nakai, H., Miura, Y., Ueshiba, H., Kakiage, Y., Une, H. (2016). Small-displacement linear surface ruptures of the 2016 Kumamoto earthquake sequence detected by ALOS-2 SAR interferometry. Earth Planets Space 68(1), 160. https://doi.org/10.1186/s40623-016-0534-x

Fukuda, J., Johnson, K.M., Larson, K.M., Miyazaki, S. (2009). Fault friction parameters inferred from the early stages of afterslip following the 2003 Tokachi-oki earthquake. J. Geophys. Res. 114(B4). https://doi.org/10.1029/2008JB006166

Gold, R.D., Reitman, N.G., Briggs, R.W., Barnhart, W.D., Hayes, G.P., Wilson, E. (2015). On- and off-fault deformation associated with the September 2013 Mw 7.7 Balochistan earthquake: Implications for geologic slip rate measurements. Tectonophysics 660, 65–78. https://doi.org/10.1016/j.tecto.2015.08.019

Gomberg, J., Johnson, P. (2005). Dynamic triggering of earthquakes. Nature 437, 830. https://doi.org/10.1038/437830a

Gualandi, A., Serpelloni, E., Belardinelli, M.E. (2014). Space–time evolution of crustal deformation related to the Mw 6.3, 2009 L'Aquila earthquake (central Italy) from principal component analysis inversion of GPS position time-series. Geophys. J. Int. 197, 174–191. https://doi.org/10.1093/gji/ggt522

Harnessing the GPS Data Explosion for Interdisciplinary Science [WWW Document], Eos. URL https://eos.org/project-updates/harnessing-the-gps-data-explosion-for-interdisciplinary-science (accessed 5.14.2019).

Hao, J., C. Ji, and Z. Yao (2016), Slip history of the 2016 Mw 7.0 Kumamoto earthquake: Intraplate rupture in complex tectonic environment, Geophys. Res. Lett., 43, doi:10.1002/2016GL071543.

Helmstetter, A., Shaw, B.E. (2009). Afterslip and aftershocks in the rate-and-state friction law. J. Geophys. Res. Solid Earth 114(B1). https://doi.org/10.1029/2007JB005077

Hill, E.M., Borrero, J.C., Huang, Z., Qiu, Q., Banerjee, P., Natawidjaja, D.H., Elosegui, P., Fritz, H.M., Suwargadi, B.W., Pranantyo, I.R. and Li, L. (2012). The 2010 Mw 7.8 Mentawai earthquake: Very shallow source of a rare tsunami earthquake determined from tsunami field survey and near-field GPS data. *Journal of Geophysical Research: Solid Earth*, *117*(B6). https://doi.org/10.1029/2012JB009159

Hreinsdóttir, S., Freymueller, J.T., Bürgmann, R. and Mitchell, J. (2006). Coseismic deformation of the 2002 Denali fault earthquake: Insights from GPS measurements. *Journal of Geophysical Research: Solid Earth*, *111*(B3). doi: 10.1029/2005JB003676

Huang, M.H., Fielding, E.J., Dickinson, H., Sun, J., Gonzalez-Ortega, J.A., Freed, A.M. and Bürgmann, R. (2017). Fault geometry inversion and slip distribution of the 2010 Mw 7.2 El Mayor-Cucapah earthquake from geodetic data. *Journal of Geophysical Research: Solid Earth*, *122*(1), pp.607-621. https://doi.org/10.1002/2016JB012858

Hyvärinen, A., Oja, E. (2000). Independent component analysis: algorithms and applications. Neural Netw. 13, 411–430. https://doi.org/10.1016/S0893-6080(00)00026-5

Ikeda, M., Toda, S., Kobayashi, S., Ohno, Y., Nishizaka, N., & Ohno, I. (2009). Tectonic model and fault segmentation of the Median Tectonic Line active fault system on Shikoku, Japan. *Tectonics*, *28*(5). https://doi.org/10.1029/2008TC002349

Jiang, H., Feng, G., Wang, T., Bürgmann, R. (2017). Toward full exploitation of coherent and incoherent information in Sentinel-1 TOPS data for retrieving surface displacement: Application to the 2016 Kumamoto (Japan) earthquake. *Geophysical Research Letters*, *44*(4), 1758-1767. https://doi.org/10.1002/2016GL072253

Kaneko, Y., Fialko, Y. (2011). Shallow slip deficit due to large strike-slip earthquakes in dynamic rupture simulations with elasto-plastic off-fault response. Geophys. J. Int. 186, 1389–1403. https://doi.org/10.1111/j.1365-246X.2011.05117.

Kato, A., Fukuda, J., Nakagawa, S., Obara, K. (2016). Foreshock migration preceding the 2016 Mw 7.0 Kumamoto earthquake, Japan. Geophys. Res. Lett. 43, 8945–8953. https://doi.org/10.1002/2016GL070079

Kobayashi, H., Koketsu, K., Miyake, H. (2017). Rupture processes of the 2016 Kumamoto earthquake sequence: Causes for extreme ground motions. Geophys. Res. Lett. 44, 6002–6010. https://doi.org/10.1002/2017GL073857

Kositsky, A.P., Avouac, J.-P. (2010). Inverting geodetic time series with a principal component analysis-based inversion method. J. Geophys. Res. Solid Earth 115(B3). https://doi.org/10.1029/2009JB006535

Lange, D., Bedford, J.R., Moreno, M., Tilmann, F., Baez, J.C., Bevis, M., Krüger, F. (2014). Comparison of postseismic afterslip models with aftershock seismicity for three subduction-zone earthquakes: Nias 2005, Maule 2010 and Tohoku 2011. Geophys. J. Int. 199, 784–799. https://doi.org/10.1093/gji/ggu292

Le, Q.V., Karpenko, A., Ngiam, J., Ng, A.Y. (2011). ICA with Reconstruction Cost for Efficient Overcomplete Feature Learning, in: Shawe-Taylor, J., Zemel, R.S., Bartlett, P.L., Pereira, F., Weinberger, K.Q. (Eds.), Advances in Neural Information Processing Systems 24. Curran Associates, Inc., pp. 1017–1025.

Leprince, S., Ayoub, F., Klinger, Y., Avouac, J. (2007). Co-Registration of Optically Sensed Images and Correlation (COSI-Corr): an operational methodology for ground deformation measurements, in: 2007 IEEE International Geoscience and Remote Sensing Symposium. Presented at the 2007 IEEE International Geoscience and Remote Sensing Symposium, pp. 1943–1946. https://doi.org/10.1109/IGARSS.2007.4423207

Liang, C. and Fielding, E.J. (2017). Interferometry with ALOS-2 full-aperture ScanSAR data. *IEEE Transactions on Geoscience and Remote Sensing*, *55*(5), pp.2739-2750. 10.1109/TGRS.2017.2653190

Lienkaemper, J.J., DeLong, S.B., Domrose, C.J., Rosa, C.M. (2016). Afterslip Behavior following the 2014 M 6.0 South Napa Earthquake with Implications for Afterslip Forecasting on Other Seismogenic Faults. Seismol. Res. Lett. 87, 609–619. https://doi.org/10.1785/0220150262

Lin, A., Chen, P., Satsukawa, T., Sado, K., Takahashi, N., Hirata, S. (2017). Millennium Recurrence Interval of Morphogenic Earthquakes on the Seismogenic Fault Zone That Triggered the 2016 Mw 7.1 Kumamoto Earthquake, Southwest JapanMillennium Recurrence Interval of Morphogenic Earthquakes. Bull. Seismol. Soc. Am. 107, 2687–2702. https://doi.org/10.1785/0120170149

Lindsey, E.O., Sahakian, V.J., Fialko, Y., Bock, Y., Barbot, S. and Rockwell, T.K., 2014. Interseismic strain localization in the San Jacinto fault zone. *Pure and Applied Geophysics*, *171*(11), pp.2937-2954.

Liu, B., Dai, W., Liu, N. (2017). Extracting seasonal deformations of the Nepal Himalaya region from vertical GPS position time series using Independent Component Analysis. Adv. Space Res., BDS/GNSS+: Recent Progress and New Applications - Part 2 60, 2910–2917. https://doi.org/10.1016/j.asr.2017.02.028

Liu, X. and Xu, W. (2019). Logarithmic Model Joint Inversion Method for Coseismic and Postseismic Slip: Application to the 2017 Mw 7.3 Sarpol Zahāb Earthquake, Iran. *Journal of Geophysical Research: Solid Earth*, *124*(11), pp.12034-12052. doi.org/10.1029/2019JB017953

Lorenzetti E, Tullis TE. (1989). Geodetic predictions of a strike-slip fault model: implications for intermediate-and short-term earthquake prediction. J. Geophys. Res. 94:12343–6. https://doi.org/10.1029/JB094iB09p12343

Ma, S. (2008). A physical model for widespread near-surface and fault zone damage induced by earthquakes: Geochem. Geophys. Geosystems 9(11). https://doi.org/10.1029/2008GC002231

Marone, C.J., Scholtz, C.H., Bilham, R. (1991). On the mechanics of earthquake afterslip. J. Geophys. Res. Solid Earth 96, 8441–8452. https://doi.org/10.1029/91JB00275

Marone, C. (1998). Laboratory-Derived Friction Laws and Their Application to Seismic Faulting. Annu. Rev. Earth Planet. Sci. 26, 643–696. https://doi.org/10.1146/annurev.earth.26.1.643

Milliner, C.W.D., Dolan, J.F., Hollingsworth, J., Leprince, S., Ayoub, F., Sammis, C.G. (2015). Quantifying near-field and off-fault deformation patterns of the 1992 Mw 7.3 Landers earthquake. Geochem. Geophys. Geosystems 16, 1577–1598. https://doi.org/10.1002/2014GC005693

Miyazaki, Larson, K.M. (2008). Coseismic and early postseismic slip for the 2003 Tokachi-oki earthquake sequence inferred from GPS data. Geophys. Res. Lett.35 (4). https://doi .org /10 .1029 /2007GL032309.

Miyakawa, A., Sumita, T., Okubo, Y., Okuwaki, R., Otsubo, M., Uesawa, S., Yagi, Y. (2016). Volcanic magma reservoir imaged as a low-density body beneath Aso volcano that terminated the 2016 Kumamoto earthquake rupture. Earth Planets Space 68, 208. https://doi.org/10.1186/s40623-016-0582-2

Moore, J.D.P., Yu, H., Tang, C.-H., Wang, T., Barbot, S., Peng, D., Masuti, S., Dauwels, J., Hsu, Y.-J., Lambert, V., Nanjundiah, P., Wei, S., Lindsey, E., Feng, L., Shibazaki, B. (2017). Imaging the distribution of transient viscosity after the 2016 Mw 7.1 Kumamoto earthquake. Science 356, 163–167. https://doi.org/10.1126/science.aal3422

Nimiya, H., Ikeda, T., Tsuji, T. (2017). Spatial and temporal seismic velocity changes on Kyushu Island during the 2016 Kumamoto earthquake. Sci. Adv. 3, e1700813. https://doi.org/10.1126/sciadv.1700813

North, G.R., Bell, T.L., Cahalan, R.F., Moeng, F.J. (1982). Sampling Errors in the Estimation of Empirical Orthogonal Functions. Mon. Weather Rev. 110, 699–706. https://doi.org/10.1175/1520-0493

Okada, Y. (1992). Internal deformation due to shear and tensile faults in a half-space. Bull. Seismol. Soc. Am. 82, 1018–1040.

Ozawa, T., Fujita, E., Ueda, H. (2016). Crustal deformation associated with the 2016 Kumamoto Earthquake and its effect on the magma system of Aso volcano. Earth Planets Space 68(1), 186. https://doi.org/10.1186/s40623-016-0563-5

Perfettini, H., Avouac, J.-P. (2007). Modeling afterslip and aftershocks following the 1992 Landers earthquake. J. Geophys. Res. Solid Earth 112(B7).

Perfettini, H., and J.-P. Ampuero (2008), Dynamics of a velocity strengthening fault region: Implications for slow earthquakes and postseismic slip, J. Geophys. Res., 113, B09411, doi:10.1029/2007JB005398. doi.org/10.1029/2006JB004399

Petit, G., Luzum, B., 2010. IERS Conventions (2010) (No. IERS-TN-36). Bureau International Des Poids Et Measures Sevres (France).

Pitarka, A., Dalguer, L.A., Day, S.M., Somerville, P.G., Dan, K. (2009). Numerical Study of Ground-Motion Differences between Buried-Rupturing and Surface-Rupturing EarthquakesNumerical Study of Ground-Motion Differences between Buried-Rupturing and Surface-Rupturing Earthquakes. Bull. Seismol. Soc. Am. 99, 1521–1537. https://doi.org/10.1785/0120080193

Platt, J.P., Leggett, J.K. and Alam, S., 1988. Slip vectors and fault mechanics in the Makran accretionary wedge, southwest Pakistan. *Journal of Geophysical Research: Solid Earth*, *93*(B7), pp.7955-7973.

Pollitz, F.F. (2001). Mantle Flow Beneath a Continental Strike-Slip Fault: Postseismic Deformation After the 1999 Hector Mine Earthquake. Science 293, 1814–1818. https://doi.org/10.1126/science.1061361

Pollitz, F.F., Kobayashi, T., Yarai, H., Shibazaki, B., Matsumoto, T. (2017). Viscoelastic lower crust and mantle relaxation following the 14–16 April 2016 Kumamoto, Japan, earthquake sequence. Geophys. Res. Lett. 44, 8795–8803. https://doi.org/10.1002/2017GL074783

Ragon, T., Sladen, A., Bletery, Q., Vergnolle, M., Cavalié, O., Avallone, A., Balestra, J. and Delouis, B. (2019). Joint Inversion of Coseismic and Early Postseismic Slip to Optimize the Information Content in Geodetic Data: Application to the 2009 M w 6.3 L'Aquila Earthquake, Central Italy. *Journal of Geophysical Research: Solid Earth*, *124*(10), pp.10522-10543.

Rockwell, T.K., Lindvall, S., Dawson, T., Langridge, R., Lettis, W., Klinger, Y. (2002). Lateral Offsets on Surveyed Cultural Features Resulting from the 1999 İzmit and Düzce Earthquakes, Turkey. Bull. Seismol. Soc. Am. 92, 79–94. https://doi.org/10.1785/0120000809

Ross, Z.E., White, M.C., Vernon, F.L., Ben-Zion, Y. (2016). An Improved Algorithm for Real-Time S-Wave Picking with Application to the (Augmented) ANZA Network in Southern CaliforniaImproved Algorithm for Real-Time S-Wave Picking with Application to ANZA. Bull. Seismol. Soc. Am. 106, 2013–2022. https://doi.org/10.1785/0120150230

Rousset, B., Barbot, S., Avouac, J.-P., Hsu, Y.-J. (2012). Postseismic deformation following the 1999 Chi-Chi earthquake, Taiwan: Implication for lower-crust rheology J. Geophys. Res. Solid Earth 117(B12). https://doi.org/10.1029/2012JB009571

Sagiya, T., S. Miyazaki, and T. Tada (2000), Continuous GPS array and present-day crustal deformation of Japan, Pure Appl. Geophys., 157, 2303–2322.

Scholz CH. (1988). The critical slip distance for seismic faulting. Nature 336:761–63. https://doi.org/10.1038/336761a0

Scott, C., Champenois, J., Klinger, Y., Nissen, E., Maruyama, T., Chiba, T., Arrowsmith, R., (2016) 2016 M7 Kumamoto, Japan, Earthquake Slip Field Derived From a Joint Inversion of Differential Lidar Topography, Optical Correlation, and InSAR Surface Displacements. Geophys. Res. Lett. *46*(12), 6341-6351. https://doi.org/10.1029/2019GL082202

Scott, C.P., Arrowsmith, J.R., Nissen, E., Lajoie, L., Maruyama, T., Chiba, T. (2018). The M7 2016 Kumamoto, Japan, Earthquake: 3-D Deformation Along the Fault and Within the Damage Zone Constrained From Differential Lidar Topography. J. Geophys. Res. Solid Earth 123, 6138–6155. https://doi.org/10.1029/2018JB015581

Serpelloni, E., Faccenna, C., Spada, G., Dong, D., Williams, S.D.P. (2013). Vertical GPS ground motion rates in the Euro-Mediterranean region: New evidence of velocity gradients at different spatial scales along the Nubia-Eurasia plate boundary. J. Geophys. Res. Solid Earth 118, 6003–6024. https://doi.org/10.1002/2013JB010102

Shelly, D.R., Hardebeck, J.L., Ellsworth, W.L., Hill, D.P. (2016). A new strategy for earthquake focal mechanisms using waveform-correlation-derived relative polarities and cluster analysis: Application to the 2014 Long Valley Caldera earthquake swarm. J. Geophys. Res. Solid Earth 121, 8622–8641. https://doi.org/10.1002/2016JB013437

Shirahama, Y., Yoshimi, M., Awata, Y., Maruyama, T., Azuma, T., Miyashita, Y., Mori, H., Imanishi, K., Takeda, N., Ochi, T., Otsubo, M., Asahina, D., Miyakawa, A. (2016).

Characteristics of the surface ruptures associated with the 2016 Kumamoto earthquake sequence, central Kyushu, Japan. Earth Planets Space 68, 191. https://doi.org/10.1186/s40623-016-0559-1

Somerville, P.G. (2003). Magnitude scaling of the near fault rupture directivity pulse. Phys. Earth Planet. Inter., The quantitative prediction of strong-motion and the physics of earthquake sources 137, 201–212. https://doi.org/10.1016/S0031-9201(03)00015-3

Stuart, W.D. (1988) Forecast model for great earthquakes at the Nankai Trough subduction zone. *PAGEOPH* **126,** 619–641. https://doi.org/10.1007/BF00879012

Tajima, Y., Hasenaka, T., Torii, M. (2017). Effects of the 2016 Kumamoto earthquakes on the Aso volcanic edifice. Earth Planets Space 69, 63. https://doi.org/10.1186/s40623-017-0646-y

Toda, S., Stein, R.S., Beroza, G.C. and Marsan, D. (2012). Aftershocks halted by static stress shadows. *Nature Geoscience*, *5*(6), p.410. doi.org/10.1038/ngeo1465

Toda, S., Kaneda, H., Okada, S., Ishimura, D., Mildon, Z.K. (2016). Slip-partitioned surface ruptures for the Mw 7.0 16 April 2016 Kumamoto, Japan, earthquake. Earth Planets Space 68. https://doi.org/10.1186/s40623-016-0560-8

Tse, S.T., and Rice., J.R. (1986) Crustal earthquake in stability in relation to the depth variation of frictional slip properties, J. Geophys. Res., 91, 9452-9472. https://doi.org/10.1029/JB091iB09p09452

Tsuji, T., Ishibashi, J., Ishitsuka, K., Kamata, R. (2017). Horizontal sliding of kilometre-scale hot spring area during the 2016 Kumamoto earthquake. Sci. Rep. 7. https://doi.org/10.1038/srep42947

Twardzik, C., Vergnolle, M., Sladen, A. and Avallone, A. (2019). Unravelling the contribution of early postseismic deformation using sub-daily GNSS positioning. *Scientific reports*, *9*(1), pp.1-12. /doi.org/10.1038/s41598-019-39038-z

Utsu, T., Ogata, Y., S, R., Matsu'ura (1995). The Centenary of the Omori Formula for a Decay Law of Aftershock Activity. J. Phys. Earth 43, 1–33. https://doi.org/10.4294/jpe1952.43.1

Wdowinski, S., Bock, Y., Zhang, J., Fang, P., Genrich, J. (1997). Southern California permanent GPS geodetic array: Spatial filtering of daily positions for estimating coseismic and postseismic displacements induced by the 1992 Landers earthquake. J. Geophys. Res. Solid Earth 102, 18057–18070. https://doi.org/10.1029/97JB01378

Williams Simon D. P., Bock Yehuda, Fang Peng, Jamason Paul, Nikolaidis Rosanne M., Prawirodirdjo Linette, Miller Meghan, Johnson Daniel J. (2004). Error analysis of continuous GPS position time series. J. Geophys. Res. Solid Earth 109. https://doi.org/10.1029/2003JB002741

Xu, X., Tong, X., Sandwell, D.T., Milliner, C.W.D., Dolan, J.F., Hollingsworth, J., Leprince, S., Ayoub, F. (2016). Refining the shallow slip deficit. Geophys. J. Int. 204, 1867–1886. https://doi.org/10.1093/gji/ggv563

Yagi, Y., Okuwaki, R., Enescu, B., Kasahara, A., Miyakawa, A., Otsubo, M. (2016). Rupture process of the 2016 Kumamoto earthquake in relation to the thermal structure around Aso volcano. Earth Planets Space 68, 118. https://doi.org/10.1186/s40623-016-0492-3

Yue, H., Ross, Z.E., Liang, C., Michel, S., Fattahi, H., Fielding, E., Moore, A., Liu, Z., Jia, B. (2017). The 2016 Kumamoto Mw = 7.0 Earthquake: A Significant Event in a Fault–Volcano System. J. Geophys. Res. Solid Earth 122, 9166–9183. https://doi.org/10.1002/2017JB014525

Figures

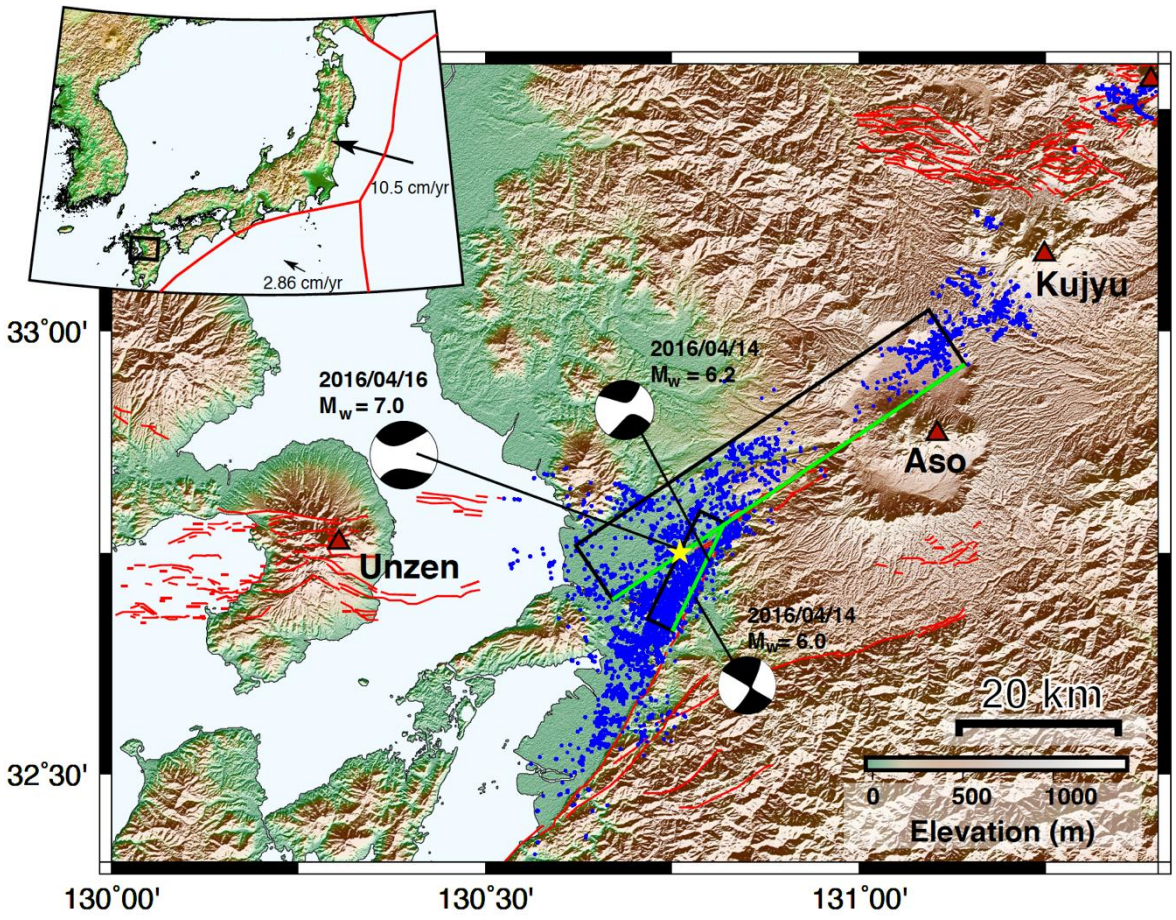

Figure 1. Location of the 2016 M_w = 7.1 Kumamoto earthquake and aftershocks on Kyushu island. GCMT solutions of the mainshock and two foreshocks are filled in black, red lines show surface traces of mapped geologic faults, blue dots show aftershocks from Yue et al. (2017), and red triangles show location of active volcanoes. The black rectangles show the fault model used in the coseismic inversion and green line the surface trace. Inset map shows the regional location in south Japan, with plate boundaries shown as red lines and plate motion as vectors relative to stable Eurasia in ITRF2014 (Argus and Gordon, 1991).

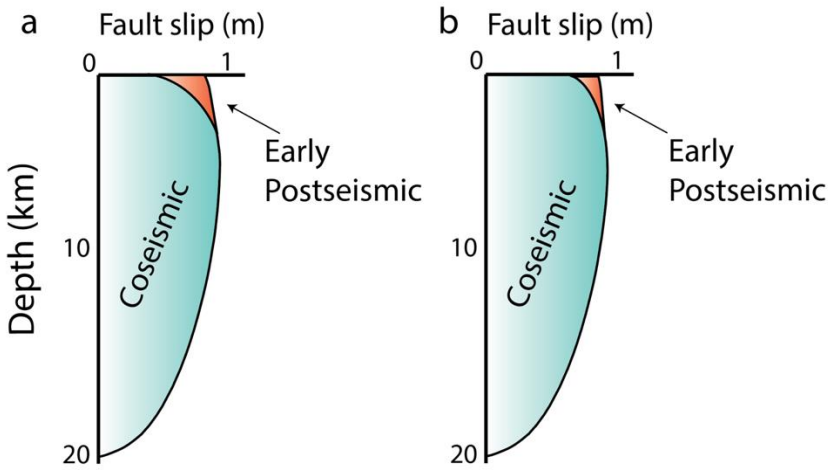

Figure 2. Simplified schematic illustrating end-member models of how early afterslip in the shallow crust may affect our understanding of coseismic slip deficits in the shallow crust (< 5 km depths). a) left shows the scenario where large coseismic slip deficits drive large and rapid afterslip, while b), right shows scenario where stored elastic strain in the shallow crust is mostly relieved coseismically with subdued coseismic slip deficits and a smaller contribution of strain release from afterslip. Distinguishing between these two endmember models requires constraining the rate of moment release as a function of depth within the first hours following rupture when afterslip rates are highest, with each model suggesting different behaviors as to how efficiently the dynamic rupture can propagate through the near-surface.

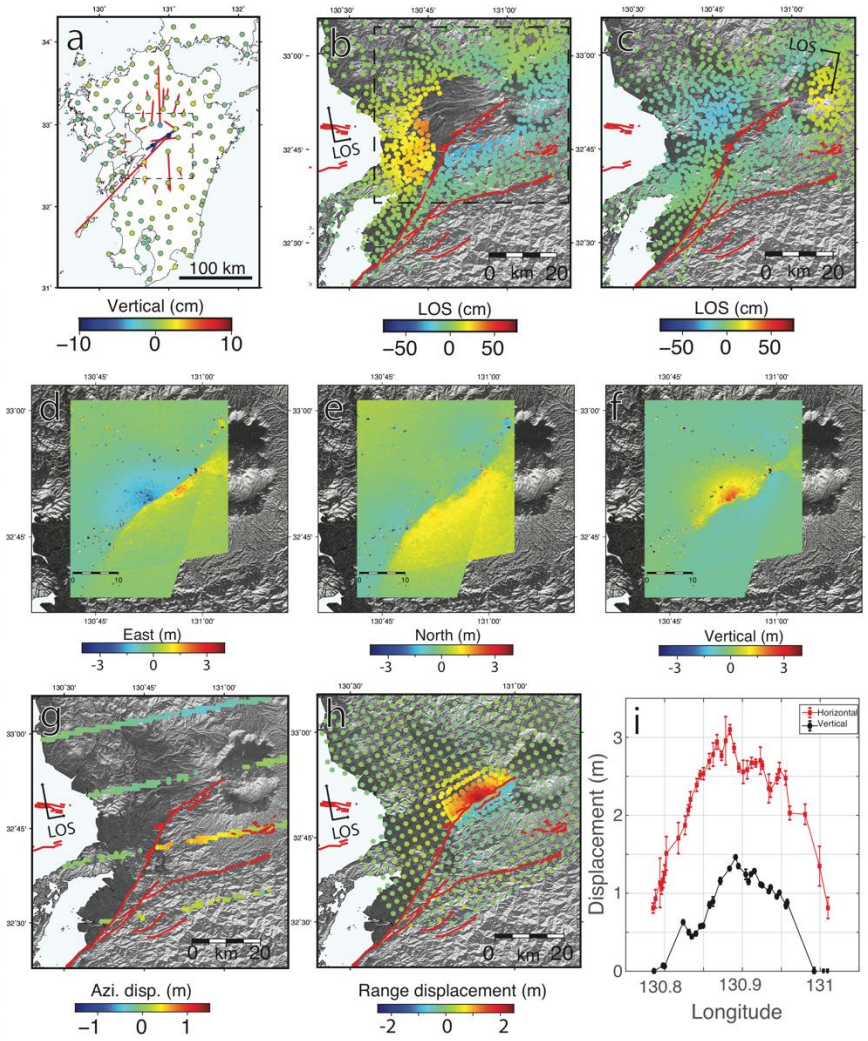

Figure 3. Geodetic data used for the coseismic slip inversion. a) and b) show ascending and descending Sentinel-1A InSAR, respectively, positive LOS is range increase c) shows horizontal (vectors) and vertical (colored dots) displacements from GPS. d-f) shows the 3D surface deformation resolved by decomposing multiple offsets maps from ALOS-2 satellite. g) and h) show azimuthal and range offset maps from Sentinel-1A imagery and i) shows the surface fault displacements, with the horizontal displacement (red line) derived from d) and e), and vertical (black line) from f).

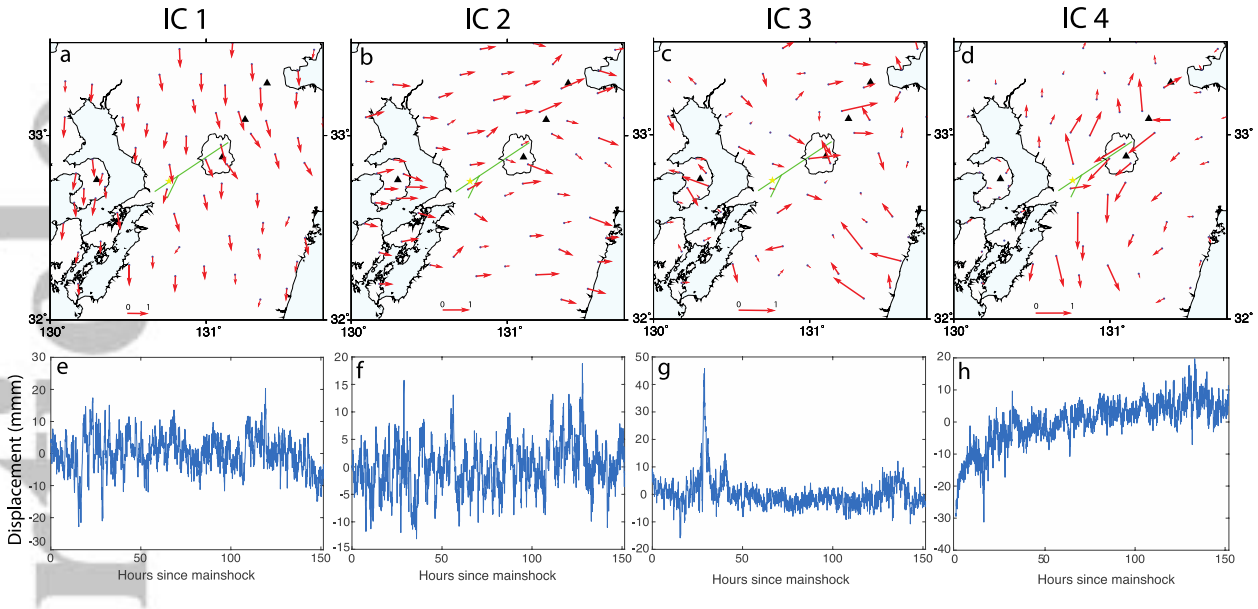

Figure 4. Independent component analysis of the five-minute sampled horizontal GPS time series during the early postseismic phase (first six days following rupture). Top row shows the spatial responses (normalized to unit scale), and bottom the temporal components. Independent components (columns) are ordered from left to right according to the amount of variance (see section S1 and eq. S1 for method). The fourth component isolates the postseismic deformation (green lines in top row show trace of Kumamoto rupture), while the first and second components represent common-mode error of the north and east motions, respectively. The third component is likely related to volcanic deformation due to the strong spatial responses (active volcanoes are shown as black triangles and Aso caldera rim is outlined with black thin line).

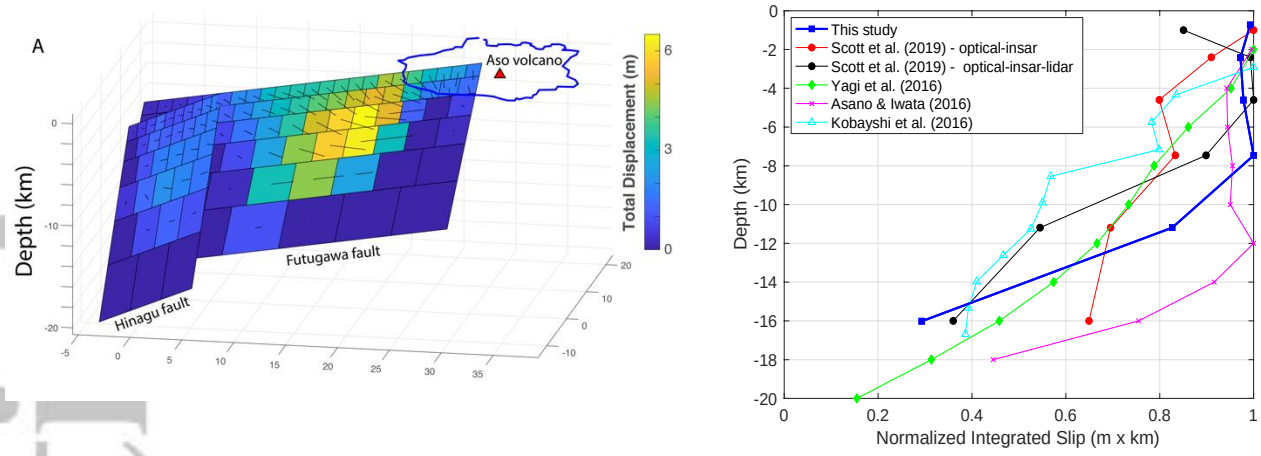

Figure 5. Oblique view towards NNW of coseismic slip model. a) The model is constrained by geodetic data shown in Figure 3 and illustrates slip variation with depth. Largest slip is located on the Futugawa fault adjacent to the Aso volcano (red triangle, with caldera rim outlined in blue). b) Slip-depth distribution from a) and comparison to other slip models. The range of behaviors illustrates the epistemic uncertainty due to use of different data and modeling approaches. Most models indicate near-surface slip is similar to that at depth, suggesting a low or almost no slip-deficit, as found in our result (thick blue line). The slip-depth curve is estimated by integrating slip at each depth interval and then normalizing by the largest value following Fialko et al. (2005).

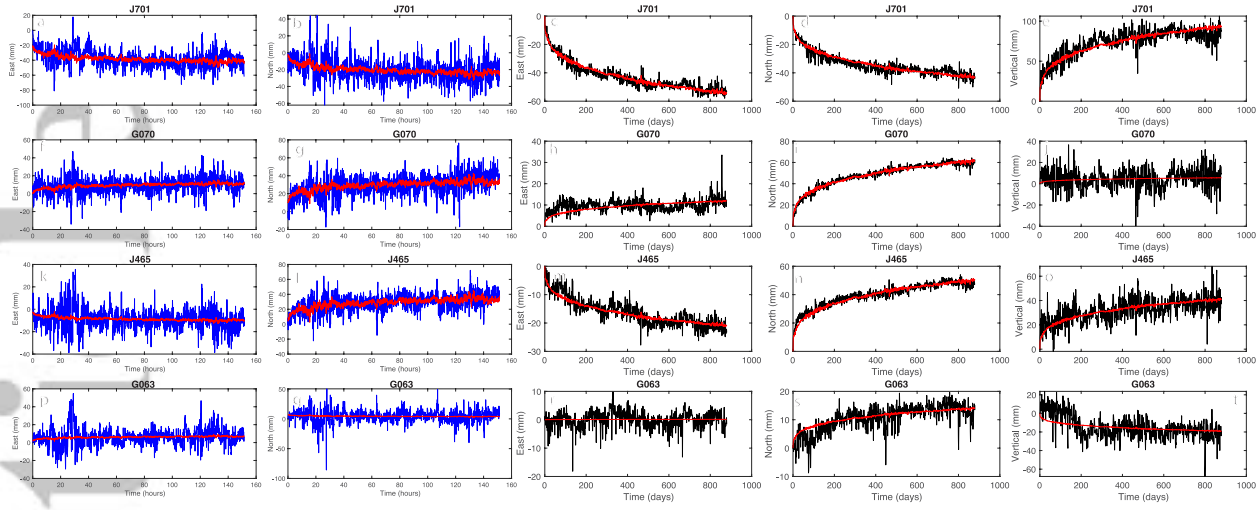

Fig 6. GPS time series of four stations (rows), of the five-minute sampled data during the first six days (left two columns), and the daily time series during the first two years (right three columns). The raw data are shown in blue and black, and the ICA filtered result in red.

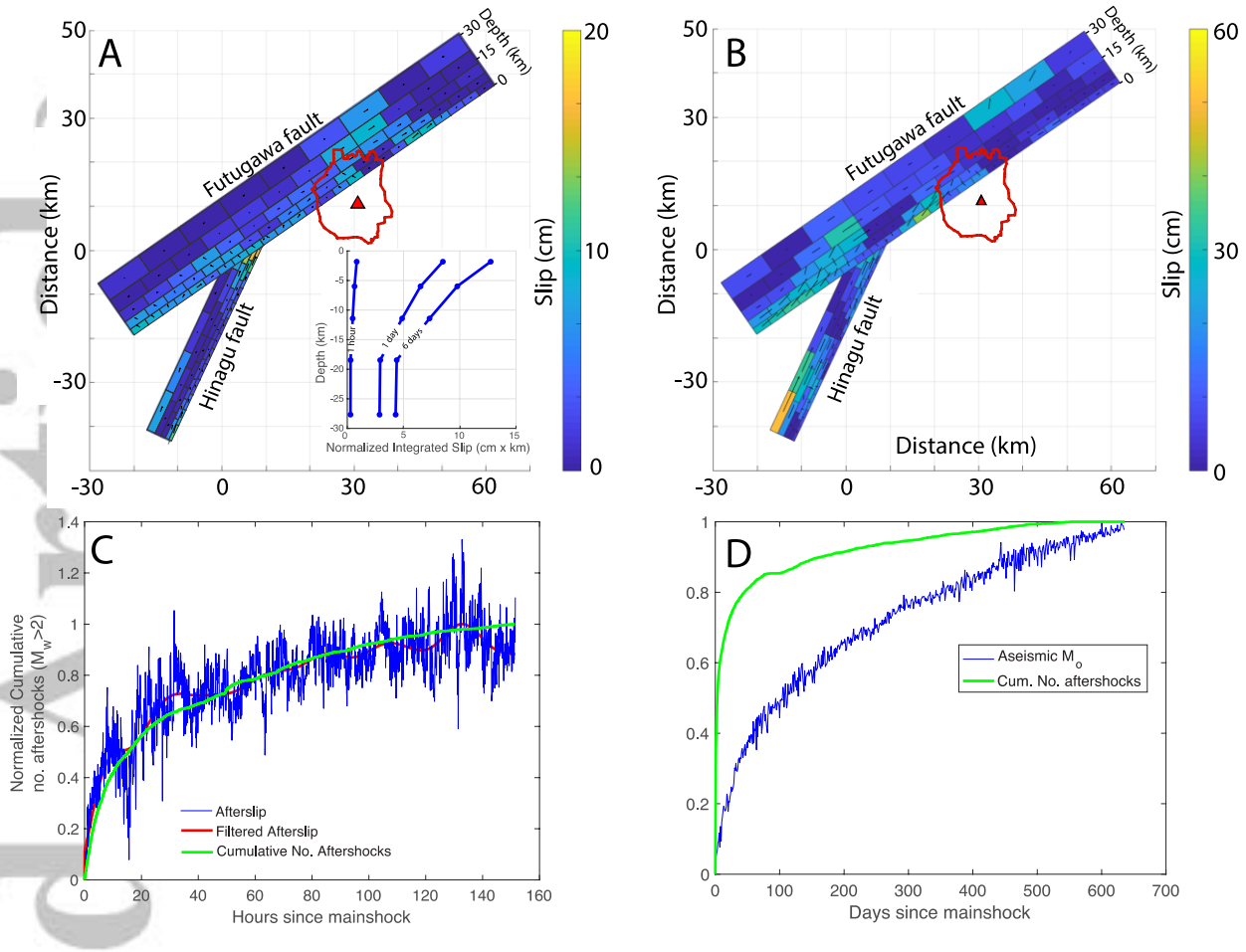

Figure 7. Results of the postseismic slip inversion. a) and b) show the slip distribution of the early postseismic phase (after the first day), and longer-term (after the first year), respectively. Inset in a) shows the evolution of the slip-depth function with time. Comparison of afterslip on a fault patch (shown in Fig. 8) versus the cumulative number of aftershocks (green lines) for the early (first six days) c) and longer-term, first two years d). Early afterslip shows good agreement with the cumulative aftershocks (with a correlation co-efficient of 0.98), while the longer-term shows a considerably weaker correlation, likely due to the effect of viscoelastic deformation biasing our afterslip model.

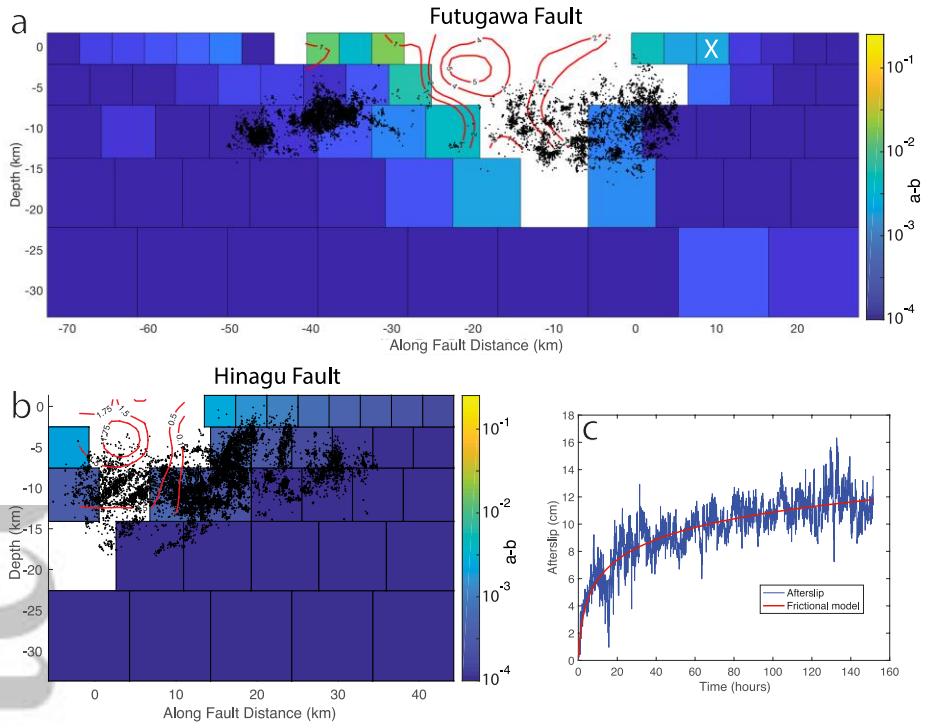

Figure 8. Estimates of frictional a-b values for each fault patch. a) and b) show a-b values for the Futugawa and Hinagu faults respectively, blank patches are those that slip coseismically and experienced a stress drop, black dots show aftershocks from the template matching catalogue within 5 km of the model fault plane, and red contours delineate slip from the coseismic model (Figure 5) (Yue et al., 2017). c) shows the fit of the frictional model (red line) from eq. (4), to afterslip (blue line) from a single patch, where the location is shown by the white X symbol in (a), on the Futugawa fault.